Spatial Consistency Calibration Based on Phase Difference Minimization for Parallel Slightly Off-Axis Digital Holographic Microscopy

Chuan Jin, Yu He, Yan Tang, Junbo Liu, Haifeng Sun, and Song Hu

***Abstract*—In this study, we propose a spatial consistency calibration method for slightly off-axis digital holographic microscopy (SO-DHM). The acquisition of relative position errors is summarized into a solution of a nonlinear optimization problem in which the root mean squared error of phase aberration of holograms is minimized. The particle swarm optimization algorithm is chosen to solve this optimization problem due to its simple structure, high convergence efficiency, and robust global search ability. Phase-only wavefronts based on phase aberration, which remove the influence of noise, are used for calibration. The simulation result indicates that the proposed method has subpixel-level precision, and the experiment demonstrates the effectiveness of the proposed method in the SO-DHM system.**

***Index Terms*—Digital holographic microscope, particle swarm optimization algorithm, slightly off-axis, spatial consistency calibration.**

I. Introduction

In RECENT years, digital holographic microscopy (DHM), as a quantitative phase imaging technique with wide-field, noncontact, and label-free advantages, has increasingly become a robust measurement tool for probing biological samples, micronano-structure detection, fluid field analysis, etc. [1]–[3]. According to the intersection angle between the object and reference waves, DHM is generally constructed with three interferometric layouts: in-line, off-axis, and slightly off-axis [4]–[6]. As an intermediate implementation of the in-line and off-axis layouts, the DC term of slightly off-axis hologram overlaps with the real and twin image terms, but the two cross-correlation terms are nonoverlapping in the spatial frequency domain. Compared with the in-line layout, slightly off-axis DHM (SO-DHM) provides faster image acquisition efficiency because of fewer phase-shifting steps. In addition, SO-DHM makes better use of the space-bandwidth of a charge-coupled device (CCD) than the off-axis layout due to the carrier frequency reduction. However, the conventional SO-DHM needs to capture two holograms successively, which is unsuitable for the dynamic measurement of samples. To improve the real time of SO-DHM, many single exposure-based simultaneous phase-shifting methods have been proposed, including Multi-Camera scheme, Pixelated mask scheme and Single-Camera scheme. Multi-Camera [7] scheme requires simultaneous control of multiple cameras, Pixelated mask scheme [8]–[9] needs to custom micro-polarization mask, and which is difficult to assemble with camera. Due to the advantange of simple structure and low cost, Single-Camera scheme has become the most general implementation scheme for parallel phase-shifting, which records several holograms with phase-shifting in different positions of a single CCD using different beam splitting components, such as grating, beam splitter, and Wollaston prism [10]–[12]. However, this scheme has a spatial mismatch problem because of the unknown spatial relative positions of captured holograms, which reduces the quality of subsequent reconstruction.

To solve the spatial mismatch problem, Kiire *et al.* [13] made fringe visibilities the same by removing the phase-shifting of holograms, and then the calibration was completed by intensity difference calculations. Millerd *et al.* [14] realized the calibration by calculating the position of the centroid of the same target. Hahn *et al.* [15] used a genetic algorithm to optimize the cost function based on intensity information. These methods rely on the image grayscale, but a series of imaging errors, including speckle noise, parasitic stripe, or inconsistent beam intensity, can drastically affect the accuracy of the calibration. Further, Li *et al.* [16] introduced circular carriers to achieve calibration parameters, but this method could not be used for some measurement scenarios where circular carriers could not be introduced. Zheng *et al.* [17] proposed a partial phase correlation (PPC) calibration method with pixel-level precision, wherein images are shifted pixel by pixel, to register spatial positions. Besides, these techniques did not consider the longitudinal position error due to the inclination of the CCD plane.

In this study, a novel spatial consistency calibration method for parallel SO-DHM is proposed. The relative position errors between holograms are acquired in a nonlinear optimization

Manuscript received March 17, 2022; revised April 19, 2022; accepted April 29, 2022. Date of publication May 3, 2022; date of current version May 23, 2022. The work was supported in part by the National Natural Science Foundation of China under Grants 61875201, 61975211, 62005287, and 61604154, in part by Sichuan Provincial Central Government Guides Local Science and Technology Development Projects under Grant 2020ZYD020, and in part by the Outstanding Youth Science and Technology Talents Program of Sichuan under Grant 2020JDJQ0005. *(Corresponding author: Song Hu.)*

Chuan Jin and Haifeng Sun are with the University of Chinese Academy of Sciences, Beijing 100049, China, and also with the Institute of Optics and Electronics, Chinese Academy of Science, Chengdu, Sichuan 610209, China (e-mail: 843034626@qq.com; hf_sun0804@163.com).

Yu He, Yan Tang, Junbo Liu, and Song Hu are with the Institute of Optics and Electronics, Chinese Academy of Science, Chengdu, Sichuan 610209, China (e-mail: heyu@ioe.ac.cn; tangyan@ioe.ac.cn; liujunbo@ioe.ac.cn; husong@ioe.ac.cn).

Digital Object Identifier 10.1109/JPHOT.2022.3171863

This work is licensed under a Creative Commons Attribution 4.0 License. For more information, see https://creativecommons.org/licenses/by/4.0/

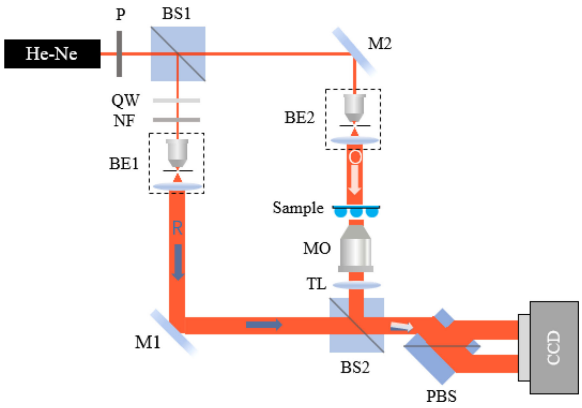

Fig. 1. Optical setup of the parallel phase-shifting SO-DHM system. P: polarizer; BS1/BS2: beam splitters; M1/M2: mirrors; QW: quarter-wave plate; NF: neural attenuator; BE1/BE2: beam expanders; MO: microscope objective; PBS: polarized beam splitter.

process when the root mean squared error (RMSE) of phase aberration of holograms from different spatial positions is minimized. The calibration modeling is performed using constructed phase-only wavefronts whose phase map is based on phase aberration with Zernike fitting, and the modeling process excludes the influence of intensity and phase noise on the results. Further, longitudinal position errors due to the inclination of the CCD plane are considered and corrected. Compared with the conventional calibration methods [13]–[17], the proposed method has subpixel-level precision and can be easily implemented.

The remainder of this article is organized as follows. Section II describes the principle of spatial mismatch and calibration procedure. Section III presents simulation results (to demonstrate the high precision of the proposed method, the PPC method [17] was employed for calibration performance comparison) and provides the experimental results. Finally, we conclude this study in Section IV.

II. Principle and Algorithm

A. Spatial Mismatch in Parallel SO-DHM

The optical setup of the parallel phase-shifting SO-DHM system using a polarization beam splitter [18] is shown in Fig. 1. A 45° linear polarized beam ($\lambda = 633\ nm$) is split by a beam splitter into two beams. The two beams are both expanded and collimated by a beam expander comprising a microscope, pinhole, and lens. One of the beams transmits a quarter-wave plate, which transforms a linearly polarized beam into a circularly polarized beam as the reference wave, and a neural attenuator is used to adjust the intensity ratio. The other beam is projected into the sample as the object wave, which is collected by a 10× microscope objective and tube lens. The object and reference waves are recombined by the beam splitter with a slight angle, and a polarized beam splitter is devoted to split the incident beams into the vertical S polarization components and horizontal P polarization components. As a result, the two holograms, which have a $\pi/2$ phase-shifting, are captured by a single CCD (resolution 1544 × 2064, pixels size 3.45 μm) in one-shot exposure simultaneously.

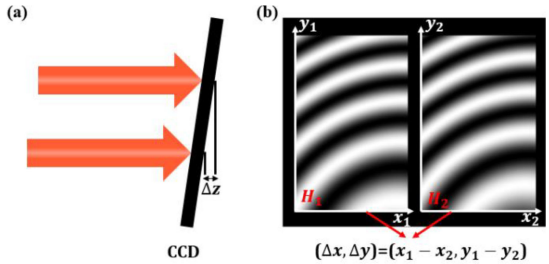

Fig. 2. The generation principle of spatial relative position errors (a and b) longitudinal and transverse position errors, respectively.

The phase-shifting holograms can be represented by

$$I_n(x,y) = |O|^2 + |R|^2 + \exp(i\alpha(n-1))O * R, + \exp(-i\alpha(n-1))OR* \quad (1)$$

where O, R, and α are the object wave, reference wave, and phase-shifting of holograms, respectively, n = 1, 2. The DC terms in the two holograms can be removed by subtracting $I_2(x,y)$ from $I_1(x,y)$:

$$I_1(x,y) - I_2(x,y) = [1 - \exp(i\alpha)]O^*R + [1 - \exp(-i\alpha)]OR^*. \quad (2)$$

To obtain the complex amplitude of the object wave, the filtering operation is implemented in a Fourier spectrum:

$$O(x,y) = IFT\{FT[(I_1 - I_2)R_D]W(u,v)\}/[1 - \exp(-i\alpha)], \quad (3)$$

where *FT* and *IFT* denote the Fourier transform and inverse Fourier transform, respectively, and R_D is the digital reference wave for phase aberration compensation; a spectrum window $W(u,v)$ is used to implement filtering operation.

The key to recovering the object wave is to ensure that the holograms are in the same relative position. However, the above steps are usually not achieved precisely due to spatial mismatch of holograms. The generation principle of spatial relative position errors is shown in Fig. 2. It is difficult to ensure that beams are incident completely perpendicular to the CCD plane, so the longitudinal position error Δz introduced due to the slight tilt of the CCD plane, which is shown in Fig. 2(a). Fig. 2(b) presents the two holograms with FOV multiplexing recorded by a single CCD in different positions, and the unknown relative positions of holograms results in transverse position error $(\Delta x, \Delta y)$ in the image segmentation process.

B. Spatial Consistency Calibration Method

Assuming that the optical axes of holograms overlap, the position relationship between hologram planes is illustrated in Fig. 3. In the Cartesian coordinate system, the second hologram in the H_2 plane as the reference plane, which is perpendicular to the z-axis, is located at the coordinate system $(x_2 - y_2)$. The first hologram in the H_1 plane in the coordinate system $(x_1 - y_1)$ is translated at $\Delta x, \Delta y, \Delta z$ with respect to the second hologram. The spatial relative position errors of holograms lead to inconsistent wavefield information in the two holograms, so numerical calculation of wavefield propagation between space planes based on the angular spectrum method is used to diffract

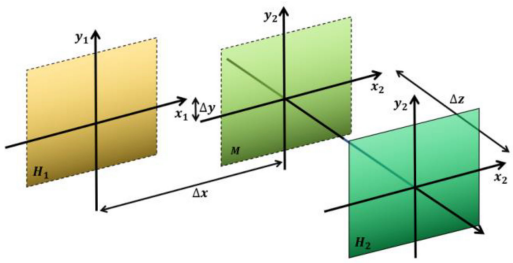

Fig. 3. Position relationship of holograms.

wavefield $h_1(x_1, y_1)$ from the H_1 plane to the H_2 plane for compensating spatial relative position errors if the position error parameters can be obtained.

$$h_1^{'}(x_2, y_2) = F\left(h_1(x_1, y_1), \Delta x, \Delta y, \Delta z\right) = IFT[FT\left(h_1(x_1, y_1)\right) \overbrace{\exp\left(-j2\pi\left(u\Delta x + v\Delta y\right)\right)}^{\text{Transverse position error compensation}} \overbrace{\exp\left(ik\Delta z\sqrt{1-(\lambda u)^2+(\lambda v)^2}\right)}^{\text{Longitudinal position error compensation}}], \tag{4}$$

where F denotes the entire spatial transformation function; u and v are the spatial frequencies in the x and y directions. The entire procedure comprises two steps. First, the translation process from the H_1 plane to the M plane is implemented to remove transverse position errors. Compared with discontinuous translation caused by the discrete characteristics of pixels in the spatial domain, this process is converted into the phase-shifting operation of the spectrum in the spatial frequency domain, which can implement subpixel-level translation. The second step is the compensation of longitudinal position errors, wherein the wavefield diffraction process between the M and H_2 planes is executed using the angular spectrum method [19].

To calculate the relative position errors $(\Delta x, \Delta y, \Delta z)$, we exploit the difference in phase aberration in the compensated hologram $h_1'(x_2, y_2)$ and the reference hologram $h_2(x_2, y_2)$ to prevent the influence of intensity noises. First, the SO-DHM system is transformed into an off-axis configuration by adjusting the tilt angle of the mirror M1, and the two holograms without a sample are recorded in the H_1 and H_2 planes. The object wavefronts without a sample can be extracted using the Fourier transform method as follows:

$$O_n(x_n, y_n) = A_n(x_n, y_n)\exp[i\varphi_n(x_n, y_n)], \tag{5}$$

where $A_n(x_n, y_n)$ is the amplitude distribution; the phase distribution $\varphi_n(x_n, y_n)$ comprises two parts: the phase noise $\varphi_m(x_n, y_n)$ and the phase aberration $\varphi_{an}(x_n, y_n)$, n = 1, 2. The phase-only wavefronts based on phase aberration $\varphi_{an}(x_n, y_n)$ can be constructed by the operation of Zernike polynomials fitting to prevent the effect of phase noise:

$$\psi_n(x_n, y_n) = \exp\left(i\varphi_{an}(x_n, y_n)\right) \approx \exp\left(i\sum_{i=1}^{9} a_i Z_i(x_n, y_n)\right), \tag{6}$$

where $Z_i(x_n, y_n)$ is the Zernike polynomial with Cartesian form, and a_i is the corresponding coefficient of the polynomial; the phase aberration can be described by 1–9 low-order Zernike polynomials. The wavefront $\psi_1(x_1, y_1)$ can be corrected by importing Eq. (4):

$$\psi_1'(x_2, y_2) = F\left(\psi_1(x_1, y_1), \Delta x, \Delta y, \Delta z\right) \tag{7}$$

The more accurate the relative position errors from the calibration process are, the more consistent $\psi_1\prime(x_2, y_2)$ and $\psi_2(x_2, y_2)$ from the H_2 plane is. The phase difference of $\psi\prime_1(x_2, y_2)$ and $\psi_2(x_2, y_2)$ is used to calculate position errors. A merit function is defined as follows:

$$P_{rmse} = \sqrt{\frac{\sum_{x=1}^{M}\sum_{y=1}^{N}\left(\varphi\prime_{a1}(x_2, y_2) - \varphi_{a2}(x_2, y_2)\right)^2}{MN}}, \tag{8}$$

where $\varphi\prime_{a1}$ is the phase of the calculated wavefront $\psi\prime_1(x_2, y_2)$. The merit function value, which is set as the RMSE of the phase distribution, can be minimized if the position errors are compensated. Hence, the spatial relative position errors $(\Delta x\prime, \Delta y\prime, \Delta z\prime)$ can be acquired by solving the following nonlinear multivariable optimization problem:

$$(\Delta x', \Delta y', \Delta z') = \arg\min P_{rmse}(\Delta x, \Delta y, \Delta z) \tag{9}$$

The mainstream optimization algorithms for solving nonlinear optimization problems are the gradient-based and heuristic algorithms; the conventional gradient-based algorithms mainly include the steepest descent [20], gradient descent [21], and conjugate gradient [22] algorithms. However, it is difficult and time-consuming to calculate the gradient of the complex merit function with gradient-based algorithms. The particle swarm optimization (PSO) algorithm, as a classical heuristic algorithm, has the characteristics of a simple structure, high convergence efficiency, and strong global search ability. Owing to the superior optimization performance, PSO is widely used in multiple application scenarios, such as Job shop scheduling [23], artificial neural network [24], and multi-peak function optimization [25]. Therefore, we employed PSO with linear decreasing inertia weight strategy (LDW-PSO) [26] to solve the above optimization problem. In the standard PSO algorithm, a set of random particles are initialized, including the two variables of particle position m and velocity v. The position of the particle represents the relative position errors, which determines the value of the merit function. The value of the merit function is called fitness in the standard PSO. The smaller the fitness, the higher the calibration accuracy. The particle velocity determines the step length and searches the direction of each iteration of particles, and then iterative optimization is performed by tracking the two optimal particles with the smallest fitness. The two optimal values include the optimal value of the individual position of the particle itself P_{best} during multiple iterations and the optimal value of the global position of the entire population G_{best}. According to these two optimal values, the particles update their velocity and position as follows:

$$v(t+1) = wv(t) + c_1 r_1[P_{best}(t) - m(t)] + c_2 r_2[G_{best}(t) - m(t)] \tag{10}$$

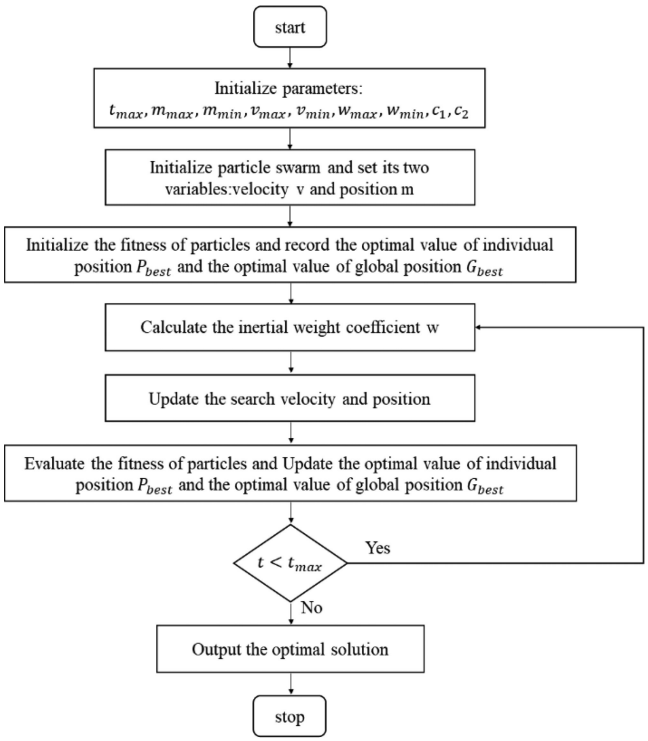

Fig. 4. The entire flow of the LDW-PSO algorithm.

$$m(t+1) = m(t) + v(t+1), \tag{11}$$

where t is the current iteration steps, c_1 and c_2 denote the self-cognitive factor and social cognitive factor, respectively; r_1 and r_2 both denote random numbers, $r_1, r_2 \in (0, 1)$; w is the inertial weight coefficient, which determines the impact of the particle's current fitness on the next search direction and step length. In this study, linear decreasing inertia weight strategy is used, which makes the inertia weight decrease from the maximum value $w_{\max}$ to the minimum value $w_{\min}$ with an increase in the number of iterations; the expression of w is as follows:

$$w(t) = w_{\max} - \frac{t(w_{\max} - w_{\min})}{t_{\max}}, \tag{12}$$

where $t_{\max}$ denotes maximum iterations. The entire flow of the LDW-PSO algorithm is illustrated in Fig. 4.

In summary, the spatial consistency calibration in the SO-DHM system comprises four steps (Fig. 5).

Step 1: The configuration of the system is adjusted to an off-axis configuration, and the holograms without samples are acquired.

Step 2: The object wave is extracted using the Fourier transform method, and the phase-only wavefronts based on Zernike fitting are constructed.

Step 3: The calibration problem is transformed into a nonlinear multivariable optimization problem [Eq. (9)]. The RMSE of the phase difference of the wavefronts is used as the merit function Eq. (8).

Step 4: The relative position errors $(\Delta x, \Delta y, \Delta z)$ are obtained from solving Eq. (9) with LDW-PSO.

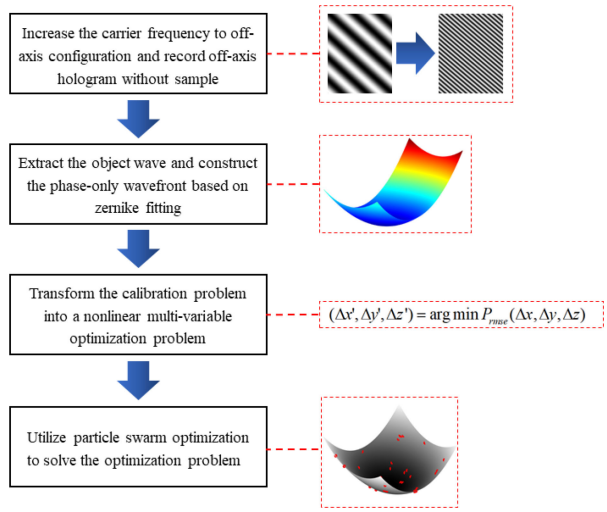

Fig. 5. The flow of the proposed calibration method.

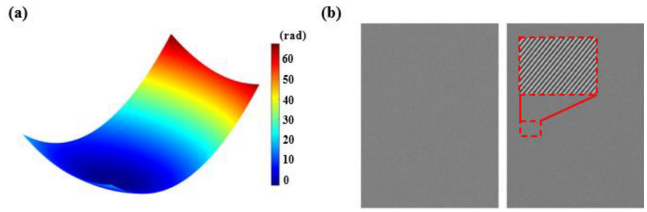

Fig. 6. (a) Introduced phase aberration; (b) Simulated $\pi/2$ phase-shifting off-axis holograms without samples.

TABLE I
SIMULATION DATA OF THE RELATIVE POSITION ERROR

	Δx / *pixel*	Δy / *pixel*	Δz / *mm*
Introduced	−30.415	25.562	1.300
PPC method	−30	26	None
Proposed method	−30.410	25.568	1.298

Once the position error parameters are obtained, we adjust the system to a slight off-axis configuration, gather the two holograms with samples and compensate for the position errors using Eq. (4). Finally, the object wave is reconstructed using Eq. (3).

III. SIMULATION AND EXPERIMENT

A. Simulation Analysis

To demonstrate the validity and high precision of the proposed method, we performed a numerical simulation. The phase aberration of the system is described with 1–9 low-order Zernike polynomials in ZEMAX classification [Fig. 6(a)], whose coefficients are set as [$-9e^3$, 600, $3.5e^6$, 0, $1.6e^6$, 0, 0, 0, $6.0622e^6$]. The phase maps both have a resolution of 800 × 600 pixels, and the pixel size is 3.45 μm. The two phase-shifting off-axis holograms without samples in Fig. 6(b) are generated for calibration. The relative position errors between two holograms, which are presented in the second row of Table I, are introduced. Meanwhile, these holograms are both added random intensity and phase noise of normal distribution with a maximum of 10%.

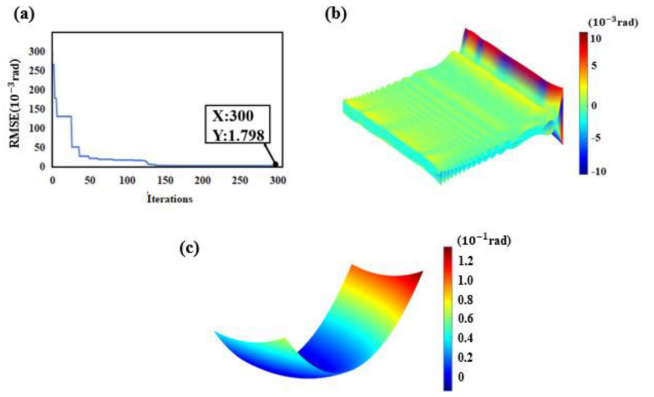

Fig. 7. Simulation results: (a) the convergence curve of RMSE of the phase distribution based on LDW-PSO; (b) the entire phase difference distribution using the proposed method; (c) the entire phase difference distribution using the PPC method.

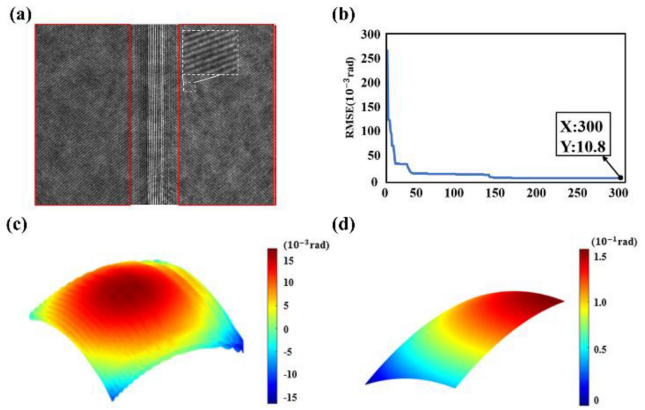

Fig. 8. The calibration results. (a) Off-axis holograms without samples; (b) the convergence curve of RMSE of the phase distribution based on LDW-PSO; (c) the whole phase difference distribution using our proposed method; (d) the whole phase difference distribution using PPC method.

The PPC method [17] and proposed method were employed to obtain the relative position errors. The calibration results of the PPC method are shown in the third row of Table I. Owing to the limitation of the PPC method in principle, transverse position errors with pixel precision were acquired, whereas the longitudinal position errors were ignored. In the simulation of the proposed method, the particle dimension was 3, the particle swarm size was 30 for ensuring the optimization speed and precision, The self-cognitive factor c_1 and social cognitive factor c_2 were both set to 2.05, and linear inertia weight $w_{\max} = 0.9$ and $w_{\min} = 0.4$. Considering the accuracy of coarse alignment and the convergence efficiency of PSO, the position and speed scope of transverse position errors were strictly limited to (-50 pixels, 50 pixels), and the position and speed scope of longitudinal position errors were set to (-3 mm, 3 mm). After 300 iterations of LDW-PSO, the calibration results of the proposed method were obtained (the fourth row of Table I). The difference of simulated and calibrated transverse position errors was less than 0.01 pixel, whereas that of the longitudinal position errors was 0.002 mm. Undoubtedly, the calibrated data of the proposed method are nearly identical to the introduced position errors.

In addition, the optimization curve of the merit function based on LDW-PSO is shown in Fig. 7(a). The RMSE of the phase distribution reduced from 0.265 to 1.798e^{-3} rad after 300 iterations. The entire phase difference distribution of the two wavefronts is shown in Fig. 7(b); there is a high degree of consistency between the two wavefronts. Notably, the phase difference distribution shows wavy stripes, which is because the Fourier transform operation in the simulation causes ringing artifacts. Nevertheless, the RMSE of the phase distribution using the PPC method was 0.0407 rad. The entire phase difference distribution of the two wavefronts is presented in Fig. 7(c). The above simulation proves that the proposed method has higher accuracy than the PPC method in spatial consistency calibration, even to the subpixel level.

B. Experiment Analysis

For extracting the phase aberration of the system illustrated in Fig. 1, the mirror M1 is adjusted to off-axis geometry. The two off-axis holograms without samples, which are segmented roughly in red rectangles, are recorded as shown in Fig. 8(a). Owing to the imaging characteristics of the system, the two holograms symmetrically distribute along the central dark region of an image, and it is necessary to implement the flip operation for one of the holograms.

TABLE II
EXPERIMENTAL DATA OF THE RELATIVE POSITION ERROR

	Δx / *pixel*	Δy / *pixel*	Δz / *mm*
PPC method	18	1	None
Proposed method	18.362	1.623	0.178

The hologram on the left image is set as a reference hologram, and the proposed calibration method is used.

During the calibration, the optimization curve of the LDW-PSO-based merit function is indicated in Fig. 8(b), and the parameters in LDW-PSO are consistent with those given in the simulation. After 300 iterations, the RMSE of the phase distribution drops to 10.8e^{-3} rad, and the phase difference distribution is presented in Fig. 8(c). Compared with the simulation result, the difference of wavefronts is greater because of a small amount of fitting error generated by phase noises. However, it is undeniable that the two wavefronts still have good consistency. Meanwhile, the PPC method is used as reference of calibration results. The RMSE of the phase distribution using the PPC method was 0.052 rad. The whole phase difference distribution of the two wavefronts is presented in Fig. 8(d). The calibration results of these two methods are displayed in Table II. For different spatial positions, the RMSE value are calculated using (8), and the distribution of RMSE is shown in Fig. 9 with the spatial position range (-10 pixels, 10 pixels). As we can see from Fig. 9, the center of image is at the (18.362,1.623). The RMSE value is minimum at the center and increases with distance from the center, which means the optimization results are reliable.

After obtaining the relative position error parameters, the slightly off-axis geometry is recovered, and a microlens array (refractive index of 1.458 and average height of 5.3 μm) made of fused silica is chosen as the specimen; The slight off-axis

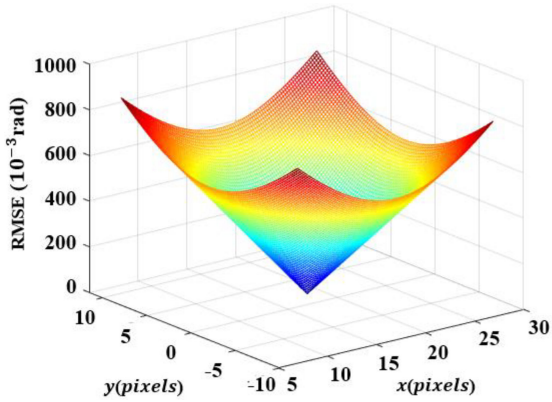

Fig. 9. the distribution of RMSE value in different spatial positions.

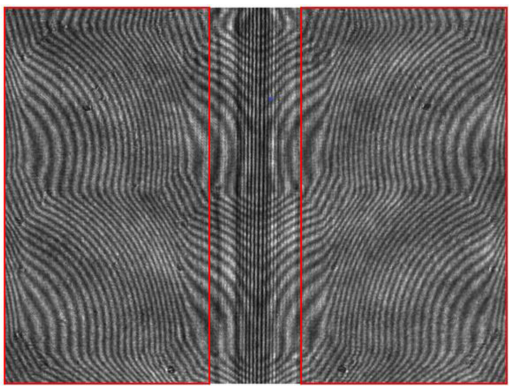

Fig. 10. The slightly off-axis holograms of microlens array.

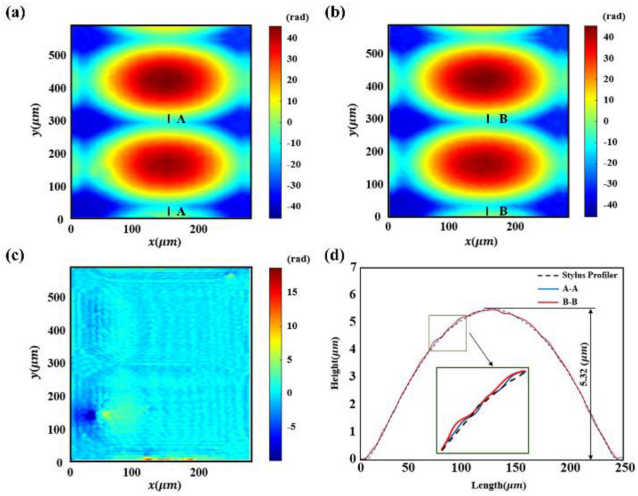

Fig. 11. Experimental results: (a) the recovered phase distribution of microlens using proposed calibration method; (b) the recovered phase distribution of microlens using PPC calibration method; (c) the phase deviation distribution between Fig.11(a) and Fig.11(b); (d) the profile through the center of microlens.

holograms of microlens are obtained, as shown in Fig. 10, and the two holograms are segmented in the same red rectangles and corrected using (4). By executing the object wave reconstruction algorithm of slightly off-axis holograms, the microlens phase distribution can be determined [Fig. 11(a)]. Fig. 11(b) shows the

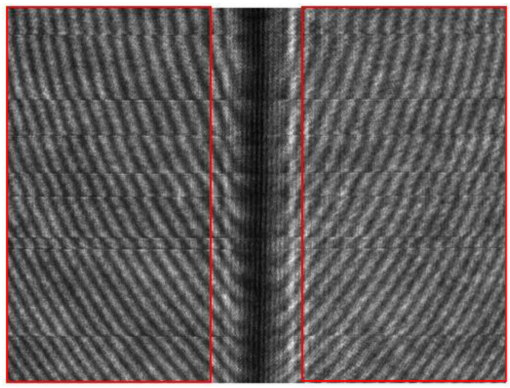

Fig. 12. The slightly off-axis holograms of aperiodic grating.

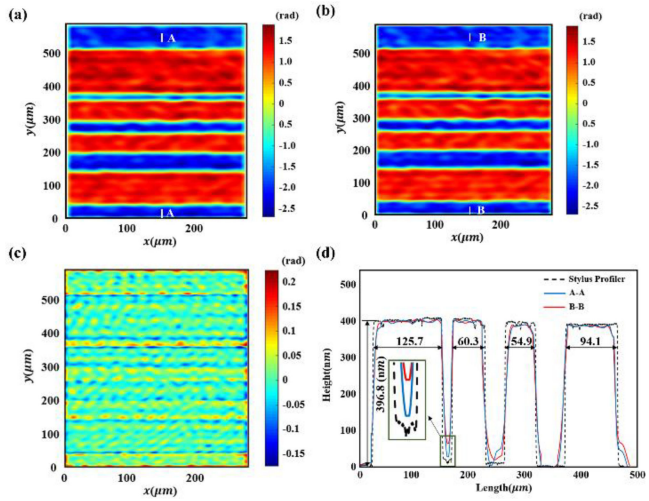

Fig. 13. Experimental results: (a) the recovered phase distribution of grating using proposed calibration method; (b) the recovered phase distribution of grating using PPC calibration method; (c) the phase deviation distribution between Fig.13(a) and Fig.13(b); (d) the profile through the center of grating.

recovered phase distribution of microlens using PPC calibration method; Compared with Fig. 11(b), the recoverd phase distribution using our proposed method has less noise and smoother surfaces. Fig. 11(c) illustrates the deviation between the two phase distributions, which manifests as wavy stripes, caused by spatial mismatch. To verify the reconstruction precision, the profile curve of the microlens measured using the stylus profiler is plotted together with the center of microlens shape in Fig. 11(a) and Fig. 11(b), as shown in Fig. 11(d). This Figure shows a very good agreement between three contours, but it can be seen from the partial enlarged image that the profile A-A based on proposed calibration method is closer to the result of profiler.

In order to guarantee the reliability of its calibration results, a aperiodic grating(refractive index of 1.458 and average height of 385 nm) is also used as sample. As shown in Fig. 12, the slight off-axis holograms of aperiodic grating are captured. According to the calibration data from proposed method and PPC method, the phase map is reconstructed respectively in Fig. 13(a) and Fig. 13(b). The phase deviation distribution between Fig. 13(a)

and Fig. 13(b) is shown in Fig. 13(c). Finally, the profile of grating using two calibration methods and profiler are shown in Fig. 13(d). The profile based on our proposed method has better consistency with the profiler result. These results demonstrate the validity and high calibration accuracy of the proposed calibration method in SO-DHM.

IV. Conclusion

In summary, spatial consistency calibration based on phase difference minimization for parallel SO-DHM is proposed. Because the calibration process uses the phase aberration of the SO-DHM system to construct phase-only wavefronts based on Zernike fitting, the intensity and phase noises in images, which can affect the calibration accuracy, are effectively removed. Further, our method considers the longitudinal position error due to the inclination of a CCD plane. The relative position error parameters are extracted by minimizing the RMSE of the phase distribution of constructed wavefronts. Simulation and experimental results demonstrate the subpixel-level precision and feasibility of the proposed calibration method. In future work, the proposed method could be extended to other nonimaging interferometer systems.

Acknowledgment

The authors sincerely thank Prof. Dong for providing the stylus profiler.

References

[1] E. Cuche *et al.*, "Simultaneous amplitude-contrast and quantitative phase-contrast microscopy by numerical reconstruction of Fresnel off-axis holograms," *Appl. Opt.*, vol. 38, no. 34, pp. 6994–7001, Dec. 1999, doi: 10.1364/AO.38.006994.

[2] J. Garcia-Sucerquia *et al.*, "4-D imaging of fluid flow with digital in-line holographic microscopy," *Optik*, vol. 119, no. 9, pp. 419–423, Jul. 2008, doi: 10.1016/j.ijleo.2007.01.004.

[3] B. Rappaz *et al.*, "Measurement of the integral refractive index and dynamic cell morphometry of living cells with digital holographic microscopy," *Opt. Exp.*, vol. 13, no. 23, pp. 9361–9373, Nov. 2005, doi: 10.1364/OPEX.13.009361.

[4] I. Yamaguchi and T. Zhang, "Phase-shifting digital holography," *Opt. Lett.*, vol. 22, no. 16, pp. 1268–1270, 1997, doi: 10.1364/ol.22.001268.

[5] E. Cuche *et al.*, "Spatial filtering for zero-order and twin-image elimination in digital off-axis holography," *Appl. Opt.*, vol. 39, no. 23, pp. 4070–4075, Aug. 2000, doi: 10.1364/AO.39.004070.

[6] N. T. Shaked *et al.*, "Two-step-only phase-shifting interferometry with optimized detector bandwidth for microscopy of live cells," *Opt. Exp.*, vol. 17, no. 18, pp. 15585–15591, Aug. 2009, doi: 10.1364/OE.17.015585.

[7] P. Sun, L. Zhong, C. Luo, W. Niu, and X. Lu, "Visual measurement of the evaporation process of a sessile droplet by dual-channel simultaneous phase-shifting interferometry," *Sci. Rep.*, vol. 5, no. 1, Dec. 2015, Art. no. 12053, doi: 10.1038/srep12053.

[8] Z. Zhang *et al.*, "Real-time phase measurement of optical vortices based on pixelated micropolarizer array," *Opt. Exp.*, vol. 23, no. 16, Aug. 2015, Art. no. 20521, doi: 10.1364/OE.23.020521.

[9] D. Wang and R. Liang, "Simultaneous polarization Mirau interferometer based on pixelated polarization camera," *Opt. Lett.*, vol. 41, no. 1, pp. 41–44, Jan. 2016, doi: 10.1364/OL.41.000041.

[10] P. Gao *et al.*, "Parallel two-step phase-shifting digital holograph microscopy based on a grating pair," *J. Opt. Soc. Amer. A Opt. Image Sci. Vis.*, vol. 28, no. 3, pp. 434–440, Mar. 2011, doi: 10.1364/JOSAA.28.000434.

[11] J. A. Picazo-Bueno *et al.*, "Single-shot slightly off-axis digital holographic microscopy with add-on module based on beamsplitter cube," *Opt. Exp.*, vol. 27, no. 4, pp. 5655–5669, Feb. 2019, doi: 10.1364/OE.27.005655.

[12] N. T. Shaked *et al.*, "Dual-interference-channel quantitative-phase microscopy of live cell dynamics," *Opt. Lett.*, vol. 34, no. 6, pp. 767–769, Mar. 2009, doi: 10.1364/OL.34.000767.

[13] T. Kiire *et al.*, "Phase-shifting interferometer based on changing the direction of linear polarization orthogonally," *Appl. Opt.*, vol. 47, no. 21, pp. 3784–3788, Jul. 2008, doi: 10.1364/AO.47.003784.

[14] J. E. N. J. Millerd, "Brock, and L. Denneau," in *Calibration Error Correct. Multi-Channel Imaging*, 2005.

[15] J. Hahn, "Spatial phase-shifting interferometry with compensation of geometric errors based on genetic algorithm," *Chin. Opt. Lett.*, vol. 7, no. 12, pp. 1113–1116, 2009, doi: 10.3788/COL20090712.1113.

[16] B. Li *et al.*, "Spatial mismatch calibration using circular carrier technique in the simultaneous phase shifting interferometry," *Appl. Opt.*, vol. 51, no. 8, pp. 1037–1044, Mar. 2012, doi: 10.1364/AO.51.001037.

[17] D. Zheng *et al.*, "Spatial mismatch calibration based on fast partial phase correlation for interferograms in dynamic Fizeau interferometer," *Opt. Eng.*, vol. 59, no. 3, Mar. 2020, Art. no. 034104, doi: 10.1117/1.OE.59.3.034104.

[18] H. Bai *et al.*, "Parallel-quadrature on-axis phase-shifting common-path interferometer using a polarizing beam splitter," *Appl. Opt.*, vol. 54, no. 32, pp. 9513–9517, Nov. 2015, doi: 10.1364/AO.54.009513.

[19] J. W. Goodman, *Introduction to Fourier Optics*. Greenwood Village, CO, USA: Roberts and Publishers, 2005.

[20] I. Yamada, "The hybrid steepest descent method for the variational inequality problem over the intersection of fixed point sets of nonexpansive mappings," *Stud. Comp. Math. Elsevier*, vol. 8, pp. 473–504, 2001, doi: 10.1016/S1570-579X(01)80028-8.

[21] K. Yuan *et al.*, "On the convergence of decentralized gradient descent," *SIAM J. Optim.*, vol. 26, no. 3, pp. 1835–1854, Jan. 2016, doi: 10.1137/130943170.

[22] Y.-H. Dai *et al.*, "On restart procedures for the conjugate gradient method," *Numer. Algorithms*, vol. 35, no. 2–4, pp. 249–260, Apr. 2004, doi: 10.1023/B:NUMA.0000021761.10993.6e.

[23] T. Jamrus *et al.*, "Hybrid particle swarm optimization combined with genetic operators for flexible job-shop scheduling under uncertain processing time for semiconductor manufacturing," *IEEE Trans. Semicond. Manuf.*, vol. 31, no. 1, pp. 32–41, Feb. 2018, doi: 10.1109/TSM.2017.2758380.

[24] J. Liu and X. Qiu, "A novel hybrid PSO-BP algorithm for neural network training," in *Proc. Int. Joint Conf. Comput. Sci. Optim.*, Sanya, Hainan, China, Apr. 2009, pp. 300–303, doi: 10.1109/CSO.2009.22.

[25] M. Li *et al.*, "A hybrid niching PSO enhanced with recombination-replacement crowding strategy for multimodal function optimization," *Appl. Soft Comput.*, vol. 12, no. 3, pp. 975–987, Mar. 2012, doi: 10.1016/j.asoc.2011.11.032.

[26] J. C. Bansal *et al.*, "Inertia weight strategies in particle swarm optimization," in *Proc. 3rd World Congr. Nature Biologically Inspired Comput.*, Salamanca, Spain, Oct. 2011, pp. 633–640, doi: 10.1109/NaBIC.2011.6089659.